Volume 11
Number 4
28 January 2023
Pages 1517–2056

Journal of Materials Chemistry A

Materials for energy and sustainability

rsc.li/materials-a

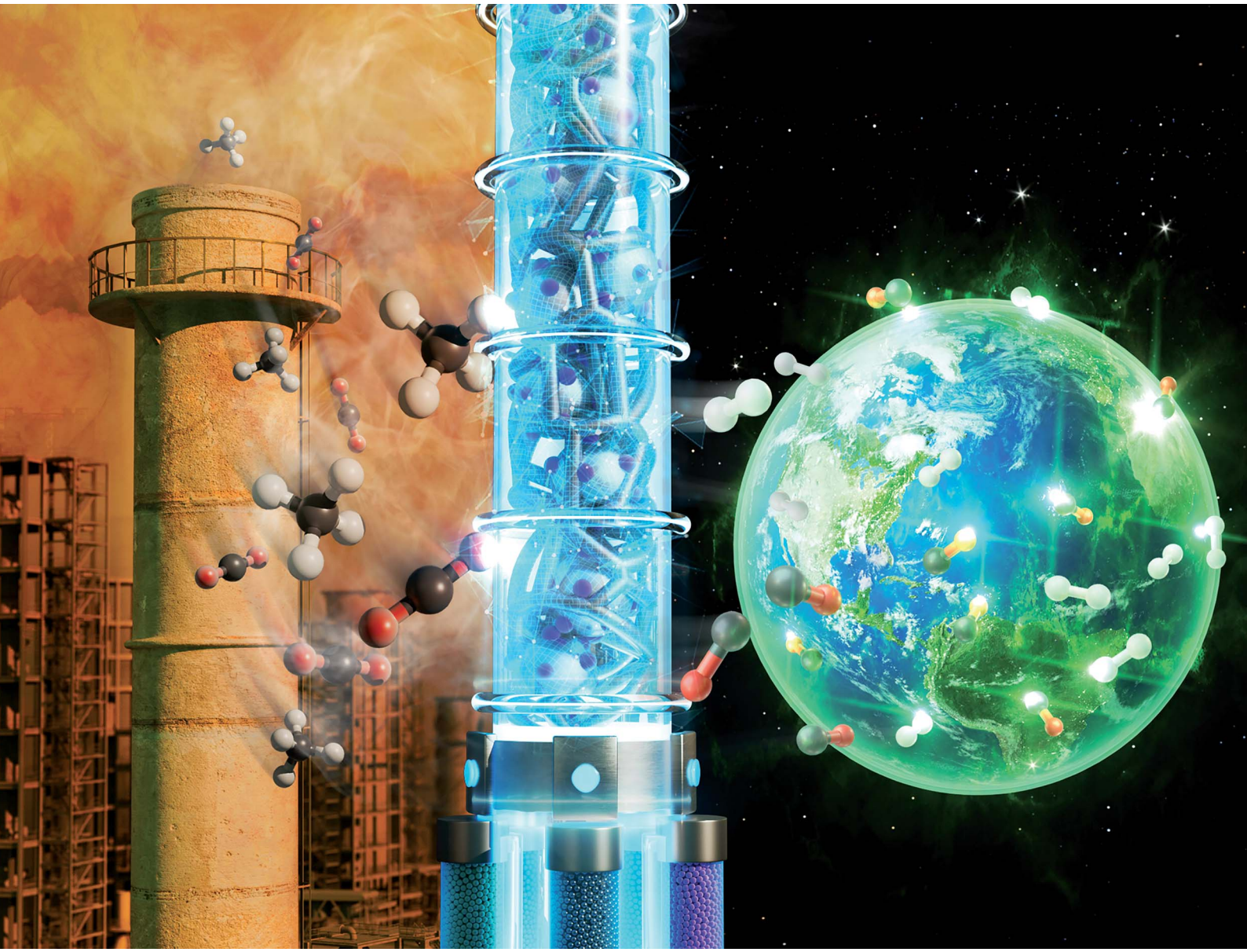

ISSN 2050-7488

ROYAL SOCIETY OF CHEMISTRY

PAPER

Chang Seop Hong, Byung-Hyun Kim, Ji Chan Park *et al.*
A new automated synthesis of a coke-resistant Cs-promoted Ni-supported nanocatalyst for sustainable dry reforming of methane

10 YEARS ANNIVERSARY

Journal of Materials Chemistry A

ROYAL SOCIETY OF CHEMISTRY

PAPER

View Article Online
View Journal | View Issue

Cite this: J. Mater. Chem. A, 2023, 11, 1666

A new automated synthesis of a coke-resistant Cs-promoted Ni-supported nanocatalyst for sustainable dry reforming of methane†

Kyung Hee Oh,[ab] Jin Hee Lee,[a] Kwangsoo Kim,[c] Hack-Keun Lee,[a] Shin Wook Kang,[a] Jung-Il Yang,[a] Jong-Ho Park,[a] Chang Seop Hong,*[b] Byung-Hyun Kim*[c] and Ji Chan Park*[ad]

Uniformly supported nanoparticles have been employed in various catalytic reactions. Recently, dry reforming of methane (DRM) has attracted much attention for reducing greenhouse gases. However, improving catalyst properties both in terms of syngas productivity and reaction stability against coke deposition is still a major issue. We report a new uniform Cs-promoted Ni/Al_2O_3 nanocatalyst with very high Ni loading and small particle sizes (*ca.* 5 nm), prepared *via* a facile melt infiltration route in an All-In-One automated apparatus designed for the synthesis of solid catalysts. The proposed nanocatalyst showed very high productivity for syngas as well as enhanced coke resistance, which enabled the reaction to proceed under extremely high space velocity conditions up to 180 NL g_{cat}^{-1} h^{-1}. The improved catalytic properties are also elucidated by computational studies.

Received 29th October 2022
Accepted 21st December 2022

DOI: 10.1039/d2ta08442b

rsc.li/materials-a

Introduction

A variety of supported metal nanocatalysts have been synthesized for environmental and energy applications.[1–3] Until now, although the synthesis technology of supported catalysts has been significantly improved, the discovery of reliable synthetic methods and advanced tools for highly uniform catalysts remains a challenge.[4–6]

Dry reforming of methane (DRM) is becoming increasingly important as an eco-friendly process to produce syngas (CO and H_2) from greenhouse gases (CH_4 and CO_2).[7,8] However, for commercialization, the low stability for carbon deposition, which hinders the accessibility of catalytically active sites by reacting substances, is a critical problem, especially for long periods and under very harsh reaction conditions.[9] Catalyst coking and pore-clogging occur very easily, reducing conversion and trapping the reaction.

High-performance catalysts for DRM have been developed for high syngas productivity and reaction stability.[10–14] To date, Ni-based nanocatalysts have been extensively studied and have demonstrated the best performance based on their high C–H bond-breaking ability.[15–17] However, it is still difficult to produce inexpensive active catalysts with a simple process that can achieve high stability against sintering and coking in high-temperature reactions.

To prevent sintering and carbon deposition for the DRM reaction, one of the ideal forms would be well-dispersed metal particles in a robust metal-oxide structure with suitable metal–support interactions and basicity.[18–22] Although highly dispersed Ni nanoparticles with high Ni loading have, thus far, received a great deal of attention, achieving high-loading catalysts has been restricted to agglomeration at reaction temperatures.[23–25] If active particle dispersion can be kept, highly Ni-loaded catalysts are good candidates in terms of increasing the number of active sites. On the other hand, several promoters such as noble metals, alkali, alkaline earth, and rare metals have been used to promote the performance regarding the activity and stability of Ni nanocatalysts.[26–30]

In recent years, automated devices and high-throughput experiments have been developed for the synthesis and evaluation of nanomaterials.[31–35] In addition, computational simulation using density functional theory (DFT) of surface reactions has become an effective tool for the design and performance elucidation of new catalysts by using energies calculated from the activation and reaction of active nanomaterial surfaces.[36–39] Here, we report a new method for the optimized synthesis of a uniform Cs-promoted Ni/Al_2O_3 nanocatalyst (U-(Cs)Ni/Al_2O_3) with highly loaded tiny Ni nanoparticles (*ca.* 5 nm, 30 wt%) using a reliable automatic system. The automatic synthesis protocol based on a melt infiltration route without the use of

[a]*Clean Fuel Laboratory, Korea Institute of Energy Research, 152 Gajeong-Ro, Daejeon, 34129, Korea. E-mail: jcpark@kier.re.kr*

[b]*Department of Chemistry, Korea University, 145 Anam-ro Seongbuk-gu, Seoul, 02841, Korea. E-mail: cshong@korea.ac.kr*

[c]*Computational Science & Engineering Laboratory, Korea Institute of Energy Research, Daejeon, 34129, Korea. E-mail: bhkim@kier.re.kr*

[d]*Advanced Energy and System Engineering, University of Science and Technology, Daejeon, 34113, Korea*

† Electronic supplementary information (ESI) available. See DOI: https://doi.org/10.1039/d2ta08442b

additional solvents has advantages such as high manufacturing speed, reproducibility, sample uniformity, and user safety.

The obtained U-(Cs)Ni/Al_2O_3 catalyst achieved extremely high syngas productivity (6.89 mol_{H2} g_{cat}^{-1} h^{-1} and 7.21 mol_{CO} g_{cat}^{-1} h^{-1}) even under extremely high space velocity conditions, as well as good stability and coke resistance. Furthermore, we demonstrate the importance of uniform dispersion in Ni active sites and Cs promoters using experimental data and DFT simulations.

Experimental section

Chemicals

Nickel(II) nitrate hexahydrate ($Ni(NO_3)_2 \cdot 6H_2O$, ≥97%, Aldrich), cesium carbonate (Cs_2CO_3, 99%, Aldrich), gamma alumina powder (γ-Al_2O_3, Alfa Aesar) and anhydrous ethanol (99%, Samchen) were used as received without further purification. A commercial FCR catalyst (Süd-Chemie) was used as a control to compare the performance with the proposed catalysts.

Synthesis of U-(Cs)Ni/Al_2O_3 nanocatalysts and the Cs-free U-Ni/Al_2O_3 catalyst

The U-(Cs)Ni/Al_2O_3 nanocatalysts were prepared by a simple melt infiltration method using a fully automated All-In-One (AIO) reaction system. Briefly, powders of γ-Al_2O_3 (0.3 g, 2.9 mmol), $Ni(NO_3)_2 \cdot 6H_2O$ (0.637 g, 2.2 mmol), and Cs_2CO_3 (15.5 mg, 0.048 mmol) were uniformly mixed with a methacrylate bead (diameter: 3/8 inch), using a high-energy ball mill (SPEX 8000M Mixer/Mill®) at 1725 rpm. After mixing for 5 min, the green powder sample was transferred to a stainless steel reactor (outer diameter: 18 mm and height: 115 mm). Next, the reactor containing the powder mixture was placed in the sample holder of the automated AIO reaction apparatus.[31] Then, the automated sequence proceeded at the set values of six steps: aging, cooling, heating, calcination, cooling, and purging (Fig. 1, Table S1, and Movie S1 in the ESI†). After completing the overall sequence, the resulting black powder was submerged in anhydrous ethanol (*ca.* 15 mL) to prevent the rapid surface oxidation of the Ni nanoparticles. For application in the DRM reaction, the prepared nanocatalyst immersed in anhydrous ethanol was simply separated using a magnet and then dried in a vacuum oven at 50 °C for 2 h. For the synthesis of the Cs-free uniform catalyst (U-Ni/Al_2O_3), all procedures and conditions were the same as those of the U-(Cs)Ni/Al_2O_3 nanocatalyst except for the exclusion of the Cs precursor.

Synthesis of IWI-(Cs)Ni/Al_2O_3 and IWI-Ni/Al_2O_3 nanocatalysts

The conventional Ni-supported nanocatalysts on γ-Al_2O_3 were manually prepared by an incipient wetness impregnation (IWI) method. The prepared Ni nanocatalysts Cs-doped and Cs-free were denoted as IWI-(Cs)Ni/Al_2O_3 and IWI-Ni/Al_2O_3, respectively. We used the same reagents as in the experiment with the AIO reaction apparatus. Typically, $Ni(NO_3)_2 \cdot 6H_2O$ dissolved in ethanol (2 mL) was impregnated into γ-Al_2O_3 powder and then dried for 2 h at room temperature in a vacuum oven. After that, the dried powder was calcined at 500 °C for 2 h under a hydrogen gas flow of 100 mL min^{-1}.

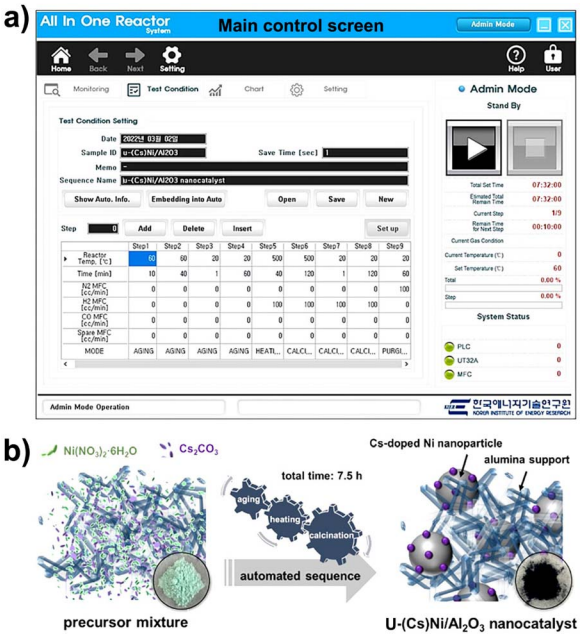

Fig. 1 (a) The main screen for the synthesis sequence set-up and (b) a brief synthetic scheme of the U-(Cs)Ni/Al_2O_3 nanocatalyst.

Dry reforming of methane reaction tests

The reaction tests were performed in a fixed-bed quartz tube reactor with an outer diameter of 1/4 inch. Some (50 mg) of the catalyst sample was loaded in the quartz reactor. Before the reaction, the catalyst was reduced *in situ* at atmospheric pressure by passing a flow of H_2 (100 mL min^{-1}) over it at 800 °C for 40 min. After reduction, a mixture of CH_4 (50 vol%) and CO_2 (50 vol%) was introduced. Then, reaction tests were carried out at 800 °C under the gas hourly space velocity (GHSV) conditions of 72 and 180 NL g_{cat}^{-1} h^{-1}, respectively. The reaction products were analyzed using a gas chromatograph (iGC7200, DS Science Inc.) equipped with a thermal conductivity detector (TCD), and catalyst activities were measured by conducting a time-on-stream study at 800 °C for 4 h. The flow rates of the outlet gases were measured using an online wet-gas flow meter (Shinagawa Co).

Computational details

We made spin-polarized density functional theory calculations using the Vienna *Ab initio* Simulation Package (VASP)[40] with the projector augmented wave (PAW) pseudopotentials,[41] and we employed the Perdew–Burke–Ernzerhof (PBE) exchange–correlation functional[42] within the generalized gradient approximation (GGA) including van der Waals corrections suggested by Grimme.[43] The Ni $4s^2 3d^8$, Cs $5s^2 5p^6 6s^1$, C $2s^2 2p^2$, O $2s^2 2p^4$ and H $1s^1$ valence electrons were treated explicitly using the Kohn–Sham equations. We further used a kinetic energy cut-off of 500 eV for plane wave expansion, and set the convergence

criteria for total electronic energy and structural optimization force to 10^{-6} eV and 0.02 eV $Å^{-1}$, respectively. A Ni (111) slab model structure with 5 layers of 6 × 6 supercells was constructed, in which the bottommost two layers were fixed while the rest of the atoms were fully relaxed. A vacuum region of 10 Å was added in the direction normal to the slab surface to avoid image–image interactions due to the periodic boundary conditions. The Brillouin zone was sampled at the Γ-point.

We calculated the adsorption energy (E_{ads}) from the following equation:

$$E_{ads} = E_{tot(molecule+substrate)} - [E_{tot(substrate)} + E_{tot(molecule)}]$$

where $E_{tot(molecule+substrate)}$ indicates the total energy of a molecule adsorbed on the substrate, and $E_{tot(substrate)}$ and $E_{tot(molecule)}$ represent the total energy of the bare substrate and the molecule in a vacuum, respectively. The zero-point energy correction, which was calculated from the vibrational frequencies for each adsorbate using finite differences, was taken into account in the adsorption energy calculations. The transition state (TS) of the reaction steps in the DRM and its activation energy were determined by the climbing image-nudged elastic band (CI-NEB) method.[44]

Characterization

Transmission electron microscopy (TEM) images were obtained using a Talos F200X operated at 200 kV. Energy-dispersive X-ray spectroscopy (EDS) elemental mapping was performed using a higher-efficiency detection system (Super X: 4 windowless SDD EDS system). High-power powder-XRD (Rigaku D/MAX-2500, 18 kW) was also used for sample analysis. X-ray photoelectron spectroscopy (XPS) was carried out using a K-alpha (TM) with a micro-focused monochromator X-ray source (Thermo VG Scientific, Inc). Hydrogen chemisorption measurement was carried out using a Micromeritics ASAP 2020C. Before measurement, the sample was heated in flowing hydrogen gas to 400 °C and was held at the same temperature for 4 h to completely reduce the catalyst. After reduction, the sample was evacuated at 150 °C for 1 h to remove any residual H_2 and cooled to 35 °C. The H_2 adsorption isotherm was recorded at 35 °C. The N_2 sorption isotherms were recorded at −196 °C with a TriStar II 3020 surface area analyzer. Before measurement, the samples were degassed in a vacuum at 300 °C for 4 h. The Ni and Cs metal concentrations in the catalyst sample were measured using inductively coupled plasma optical emission spectrometry (ICP-OES, PerkinElmer AVIO500). Temperature-programmed desorption of ammonia (NH_3-TPD) was performed using an AutoChem II 2920 instrument of Micromeritics. Before the NH_3-TPD experiment, all the samples were pretreated at 400 °C under a 50 mL min^{-1} flow of pure H_2 for 1 h to remove adsorbed water and were then saturated with 15% NH_3 under a 50 mL min^{-1} flow for 1 h at 100 °C. After the saturation step, the samples were purged with He for 30 min to eliminate weakly adsorbed ammonia from the surface of the catalysts. Finally, NH_3 desorption was performed at a ramp rate of 10 °C min^{-1} up to 700 °C under a 50 mL min^{-1} flow of pure He. Carbon deposition was quantitatively analyzed by using a thermogravimetric analyzer (TGA). TG analysis was conducted using a Setaram apparatus with a heating rate of 10 °C min^{-1} from room temperature to 800 °C under an airflow of 10 mL min^{-1}. Raman analysis was performed under a Raman microscope (Horiba LabRAM HR Evolution Visible_NIR) using a 514 nm laser.

Results and discussion

Synthesis of the U-(Cs)Ni/Al_2O_3 nanocatalyst

The AIO apparatus, which mainly consisted of a reactor, a heater, and gas controllers, was designed for user-friendly operation and highly reliable catalyst synthesis (Fig. S1†). The detailed operation of the apparatus required input of ingredients (metal precursors and metal-oxide support) and basic reaction conditions (temperature, time, active gas flow, and so on). A computer program to control the apparatus was made in the C# language (Fig. S1b†).

We prepared the U-(Cs)Ni/Al_2O_3 nanocatalyst through a simple melt infiltration method in the AIO reactor with an automatic sequence flow system.[45] The automated method, which involves aging and calcination stages, is more convenient and reliable than other conventional methods. We chose γ-Al_2O_3 as the support material because it strongly interacts with active Ni nanoparticles and has high thermal stability.[46] Because cesium as a promoter has high basicity, we selected Cs_2CO_3 as a precursor.[47] First, a mixed sample containing metal precursors and a support alumina powder was loaded into the automated AIO reaction apparatus. Next, the control program was performed to run the serial steps as the programmed sequence (Table S1†). Highly dispersed Ni nanoparticles with uniform Cs doping were prepared with a selection of several variations in the overall synthesis process, including basic steps for aging, cooling, heating, calcination, cooling, and purging, using the automated reaction system (Fig. 1a). In particular, the co-melt infiltration of the metal salts is possible in the aging step because Cs_2CO_3 salt has good water solubility (2.6 mg μL_{water}^{-1} at 15 °C). The solution from the melting of the nickel nitrate hydrate precursors at 60 °C can sufficiently dissolve the Cs salt (Fig. 1). In the whole process of the catalyst preparation, trend data in temperature, gas flow, and pressure are accumulated in real time to monitor the synthetic status (Fig. S2†). We also prepared a Cs-free U-Ni/Al_2O_3 nanocatalyst for the control experiment using the same procedure as that for U-(Cs)Ni/Al_2O_3 except that the Cs precursor was not used.

Transmission electron microscopy (TEM) and high-angle annular dark-field (HAADF)-STEM images confirmed the U-(Cs)Ni/Al_2O_3 nanocatalyst with uniform Ni particle dispersion and compact particle loading on the alumina support (Fig. 2a and S3†). In the elemental mapping image, nickel (green color) shows well-dispersed crystal domains on the aluminum matrix (red color) (Fig. 2b). Cesium (blue color) is also distributed over the Ni nanoparticles. We measured more than 200 particles in the TEM image (Fig. 2c) and confirmed the Ni particle size in the U-(Cs)Ni/Al_2O_3 catalyst to be 5.1 ± 0.7 nm. A high-resolution TEM (HR-TEM) image of the U-(Cs)Ni/Al_2O_3 nanocatalyst shows a single-crystalline Ni nanoparticle (Fig. 2d). The lattice

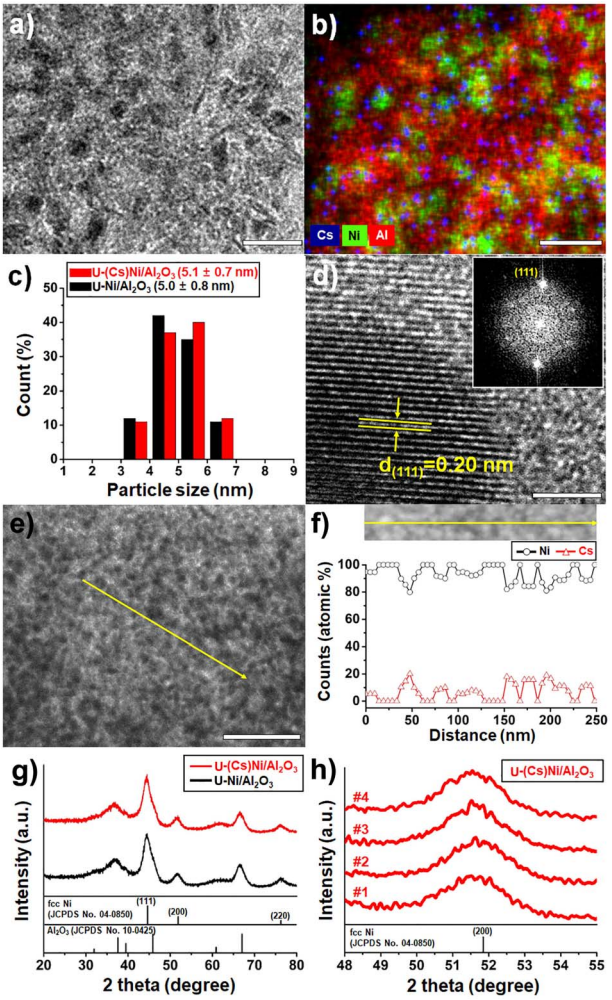

Fig. 2 (a) TEM image and (b) elemental mapping image, (c) particle size distribution histogram, (d) HR-TEM image with the corresponding FT pattern (inset), (e) low-resolution TEM image, and (f) corresponding EDX-line profile with the HAADF-STEM image of the U-(Cs)Ni/Al_2O_3 nanocatalyst. (g) XRD spectra of the uniform nanocatalysts prepared by using the AlO reactor and (h) specific XRD spectra of the U-(Cs)Ni/Al_2O_3 nanocatalysts in four different batches. The bars represent 20 nm (a and b), 2 nm (d), and 100 nm (e), respectively.

distance between neighboring fringes is 0.20 nm, which matches well with the (111) plane of metallic Ni.

The corresponding Fourier-Transform (FT) pattern also demonstrates the single-crystalline nature of Ni. The TEM and corresponding energy dispersive spectroscopy (EDS) line profile revealed that U-(Cs)Ni/Al_2O_3 exhibited uniform Cs distribution on Ni particles (Fig. 2e and f). In the X-ray diffraction (XRD) patterns of the U-(Cs)Ni/Al_2O_3 and U-Ni/Al_2O_3 nanocatalysts, the peaks well matched the reflection of face-centered-cubic (fcc) Ni (JCPDS no. 04-0850) and gamma-phase alumina (JCPDS no. 10-0425) (Fig. 2g). There were no significant differences in the XRD spectra between the Cs-free and Cs-doped samples. The average crystallite sizes of the U-(Cs)Ni/Al_2O_3 nanocatalysts in the four different batches were 4.6 ± 0.1 nm, which we estimated from the FWHM of the (200) diffraction peaks at the reflection at $2\theta = 51.8°$ (Fig. 2h).

A Cs-free Ni catalyst (U-Ni/Al_2O_3) as a control sample was prepared and analyzed in the same way. The TEM and elemental mapping images of U-Ni/Al_2O_3 showed high uniformity in Ni particle loading (Fig. S4a–d†). The single Ni nanoparticle with a spherical shape clearly showed a single-crystalline nature (Fig. S4e†). The particle size from the TEM images of the U-Ni/Al_2O_3 catalyst was slightly smaller than that of the Cs-doped one, which was determined to be 5.0 ± 0.8 nm (Fig. 2c), suggesting that the addition of the Cs salt had an insignificant effect on the final Ni particle dispersion. Similar Ni dispersions of U-Ni/Al_2O_3 and U-(Cs)Ni/Al_2O_3 in H_2 chemisorption were observed at 10.74% and 11.49%, respectively. In the XRD data, the average crystallite size of U-Ni/Al_2O_3 nanocatalysts prepared in three different batches was determined to be 4.3 ± 0.1 nm, which is slightly smaller than that (4.6 nm) of the U-(Cs) Ni/Al_2O_3 nanocatalysts (Fig. S4f†). The XRD patterns obtained from the different batches were almost identical, indicating high reproducibility of the catalyst with good reliability of the automated synthetic procedure.

The chemical structure and elemental surface state of the automated nanocatalysts were further studied using X-ray photoelectron spectroscopy (XPS). The dominant signals in the XPS spectra originated from Cs, Ni, Al, O, and C (Fig. 3a).

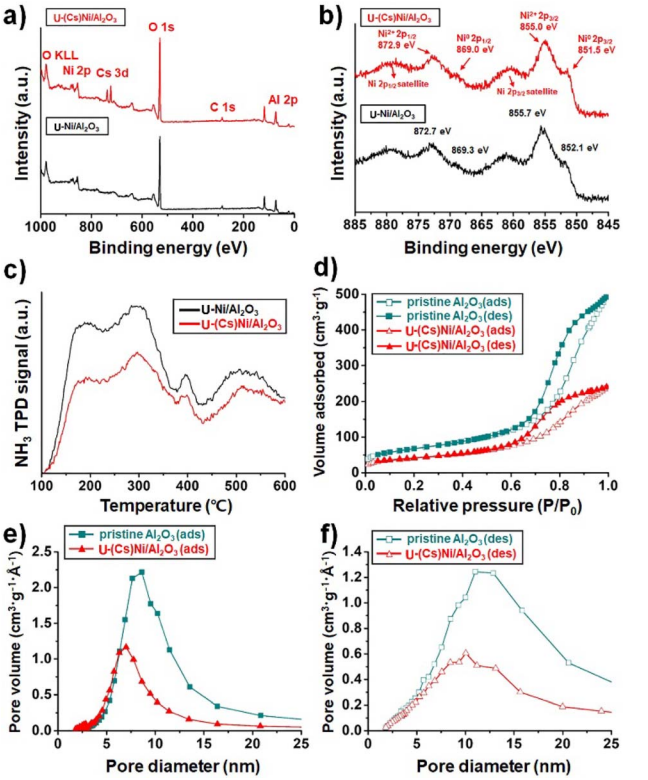

Fig. 3 XPS spectra in the energy regions of (a) the survey scan spectrum and (b) Ni 2p. (c) The acidity measurements by NH_3 adsorption using NH_3-TPD for Cs-free and Cs-doped nanocatalysts. (d) N_2 sorption isotherms of pristine Al_2O_3 and U-(Cs)Ni/Al_2O_3 nanocatalysts. Pore size distribution diagrams of the samples using the Barrett–Joyner–Halenda method by (e) adsorption and (f) desorption branches.

The nickel surfaces of the samples were mainly observed as oxidized forms,[48] although the fresh catalyst powders were readily passivated by anhydrous ethanol. The high-resolution Ni 2p XPS spectrum had two spin–orbit peaks ($2p_{1/2}$ and $2p_{3/2}$) for NiO and Ni (Fig. 3b). The Ni $2P_{3/2}$ and NiO $2P_{3/2}$ peaks for the U-(Cs)Ni/Al_2O_3 nanocatalyst were observed at 851.5 and 855.0 eV, respectively, which were lower binding energies than those of the U-Ni/Al_2O_3 nanocatalyst (852.1 and 855.7 eV). The lower binding energy of U-(Cs)Ni/Al_2O_3 was due to the increased electron density of nickel nanoparticles by Cs doped on the nickel surface. The U-(Cs)Ni/Al_2O_3 nanocatalyst also had a higher Ni^0/Ni^{2+} ratio containing more Ni^0 active sites because neighboring Cs is oxidized more easily than Ni. The XPS spectrum of the Cs band energy region had a set of peaks at 724 and 738 eV in the range of the Cs $3d_{5/2}$ and $3d_{3/2}$ orbital signals (Fig. S5†).

The adsorption properties by acid sites of the U-(Cs)Ni/Al_2O_3 and U-Ni/Al_2O_3 nanocatalysts were examined by temperature-programmed desorption of ammonia (NH_3-TPD), performed at a ramp rate of 10 °C min^{-1} up to 700 °C under a 50 mL min^{-1} flow of pure He (Fig. 3c). The peaks around 300 °C and 530 °C were related to weak and strong acidic sites, respectively. U-(Cs)Ni/Al_2O_3 had fewer acid sites in 1.01 mmol NH_3 g_{cat}^{-1} than the U-Ni/Al_2O_3 nanocatalyst (0.85 mmol NH_3 g_{cat}^{-1}).

N_2 sorption experiments on pristine Al_2O_3 and U-(Cs)Ni/Al_2O_3 were performed at −196 °C. All samples exhibited type IV adsorption–desorption hysteresis (Fig. 3d). The Brunauer–Emmett–Teller (BET) surface areas of pristine γ-Al_2O_3 and U-(Cs)Ni/Al_2O_3 were measured to be 242.2 and 150.1 m^2 g^{-1}, respectively. The total pore volume of U-(Cs)Ni/Al_2O_3 was 0.37 cm^3 g^{-1}, which is much lower than that of pristine γ-Al_2O_3 (0.76 cm^3 g^{-1}). This is because the mesopores of Al_2O_3 were almost filled with metallic Ni, which has a higher density (d = 8.908 g cm^{-3}) than Al_2O_3 (d = 3.987 g cm^{-3}). Using the Barrett–Joyner–Halenda (BJH) method on the adsorption and desorption branches, the pore sizes of pristine γ-Al_2O_3 were 11.0 nm and 8.0 nm, respectively (Fig. 3e and f). On the other hand, the reduced pore size of U-(Cs)Ni/Al_2O_3 was observed to be 10.0 nm in the adsorption branch and 7.0 nm in the desorption branch, reflecting the pores filled with Ni particles. The Cs-free U-Ni/Al_2O_3 nanocatalyst also showed similar pore properties to U-(Cs)Ni/Al_2O_3 (Fig. S6†). The BET surface area and total pore volume were 145.0 m^2 g^{-1} and 0.37 cm^3 g^{-1}, respectively.

Inductively coupled plasma optical emission spectrometry (ICP-OES) measurements showed that the Ni and Cs contents of the U-(Cs)Ni/Al_2O_3 nanocatalyst were 30.2 wt% and 2.9 wt%, respectively, which were in good agreement with the nominal values of the Ni and Cs loadings.

Catalytic performance test in dry reforming of methane

The catalytic performance of the systemically synthesized U-(Cs)Ni/Al_2O_3 and U-Ni/Al_2O_3 nanocatalysts was evaluated in dry reforming of methane (DRM) reactions by introducing a commercially available Ni-based catalyst (FCR). The main reaction was highly endothermic as follows:

$$CH_4(g) + CO_2(g) \rightarrow 2CO + 2H_2 \quad \Delta H^{\circ}_{298\,K} = 247\ kJ/mol$$

Catalytic studies were carried out in a continuous-flow quartz reactor at 800 °C with a methane (CH_4) to carbon dioxide (CO_2) ratio of 1 for 4 h time-on-stream (TOS) (Fig. S7†). CH_4 and CO_2 conversions were determined using a gas chromatograph equipped with a thermal conductivity detector. For fast performance assessment of the catalysts, reaction tests were conducted under high gas hourly space velocity (GHSV) conditions of 72 NL g_{cat}^{-1} h^{-1} and 180 NL g_{cat}^{-1} h^{-1}, respectively (Fig. 4). First, when the U-(Cs)Ni/Al_2O_3 nanocatalyst was used in the DRM reaction under GHSV = 72 NL g_{cat}^{-1} h^{-1}, very high CH_4 (89.8%) and CO_2 (91.8%) conversion rates were observed at TOS = 4 h as constant values approaching the theoretical maximum values (CH_4: 90.3% and CO_2: 94.9%) (Fig. 4a and b). The Cs-free U-Ni/Al_2O_3 nanocatalyst experienced slightly lower CH_4 and CO_2 conversions (86.9% and 88.5%) compared to the U-(Cs)Ni/Al_2O_3 nanocatalyst. On the other

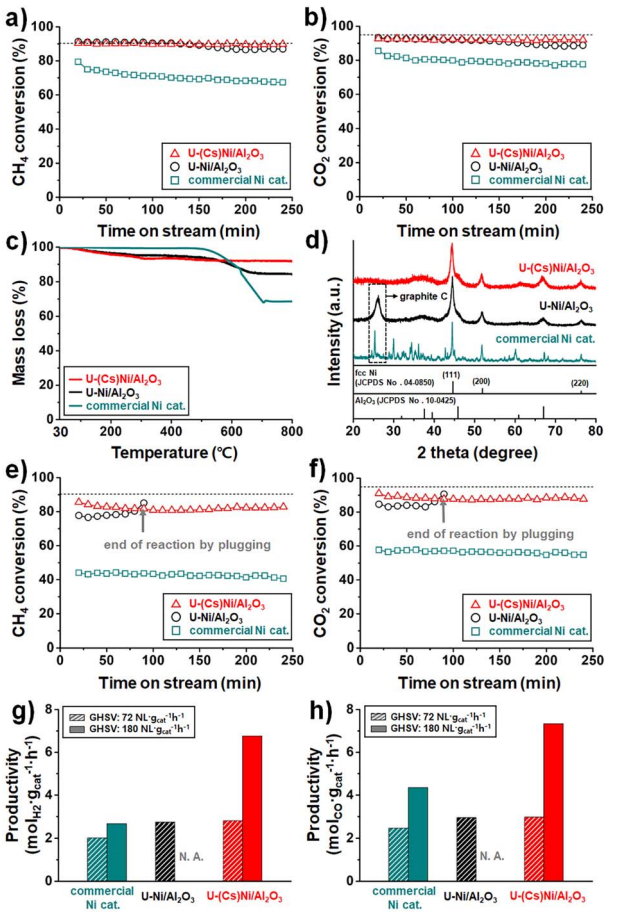

Fig. 4 (a) CH_4 and (b) CO_2 conversions of the catalysts in the DRM reaction at GHSV = 72 NL g_{cat}^{-1} h^{-1}, (c) TGA and (d) XRD data of the recovered catalysts after the DRM reactions at GHSV = 72 NL g_{cat}^{-1} h^{-1}, (e) CH_4 and (f) CO_2 conversions of the catalysts under GHSV = 180 NL g_{cat}^{-1} h^{-1} and (g) H_2 and (h) CO productivities of the catalysts. All reactions were performed at 800 °C with a CH_4/CO_2 ratio of 1. The dotted lines (a, b, e, and f) indicate the conversion rates at thermodynamic equilibrium.

hand, the commercial nickel catalyst showed a rapid deactivation tendency with low conversion rates of CH_4 67.3% and CO_2 77.6% at TOS = 4 h.

Although the conversion difference between U-Ni/Al_2O_3 and U-(Cs)Ni/Al_2O_3 was not significant at GHSV = 72 NL g_{cat}^{-1} h^{-1}, the coke resistance of the catalysts was quite different. Carbon deposition caused catalyst deactivation and reactor blockages derived from two reactions as follows:

$$CH_4 \rightarrow C_{ads} + 2H_2 \quad \Delta H^{\circ}_{298\,K} = 75\ \mathrm{kJ/mol}$$

$$2CO \rightarrow C_{ads} + CO_2 \quad \Delta H^{\circ}_{298\,K} = -172\ \mathrm{kJ/mol}$$

The carbon deposition rate (mg_{carbon} g_{cat}^{-1} h^{-1}) for the recovered catalysts after a 4 h reaction at GHSV = 72 NL g_{cat}^{-1} h^{-1} was measured by thermogravimetric analysis (TGA) (Table S2†). The TGA graphs revealed that the spent U-(Cs)Ni/Al_2O_3 nanocatalyst had a much less weight loss (1.87 wt%) than the U-Ni/Al_2O_3 nanocatalyst (12.0 wt%) and the commercial Ni catalyst (31.2 wt%) in a temperature range of 500–700 °C (Fig. 4c). In the XRD data, a broad peak ranging from 23° to 28° of the spent U-Ni/Al_2O_3 catalyst exhibited the graphitic carbon phase (JCPDS no. 75-0444), meaning that significant carbon deposition occurred in the Cs-free U-Ni/Al_2O_3 nanocatalyst during the DRM reaction (Fig. 4d).

The deposited carbon was also characterized using Raman Spectroscopy (Fig. S8†). Two strong peaks were observed at 1349 cm^{-1} and 1573 cm^{-1}, respectively, consistent with the D band and the G band. The graphitization degree was measured by calculating the I_G/I_D ratio indicating the crystallinity of the deposited carbon. The I_G/I_D value of the recovered U-Ni/Al_2O_3 nanocatalyst was 1.02, suggesting that the deposited carbon has a less ordered graphitic structure than conventional DRM catalysts.[49]

On the other hand, there was no carbon peak in the XRD spectrum of the U-Cs(Ni)/Al_2O_3 nanocatalyst, suggesting that the addition of Cs as a base promoter in the catalyst effectively suppressed the acidic sites of the catalyst surface, which can lead to carbon deposition in the DRM. Incredibly, the TEM and HAADF-STEM images with elemental mappings of the spent U-Cs(Ni)/Al_2O_3 nanocatalyst indicated high durability to sintering and carbon deposition, which was observed with the fresh catalyst (Fig. S9 and S10†). In the TEM images, there were no significant changes in particle distribution among the fresh U-Cs(Ni)/Al_2O_3, thermally treated U-Cs(Ni)/Al_2O_3 under a H_2 flow at the reaction temperature (800 °C), and the recovered U-(Cs)Ni/Al_2O_3 after the DRM reaction under GHSV = 72 NL g_{cat}^{-1} h^{-1} at 800 °C.

To maximize syngas productivity in DRM reactions, an extremely harsh space velocity condition (GHSV = 180 NL g_{cat}^{-1} h^{-1}) was applied to the catalysts. As expected, there were decreased conversion rates for all the catalysts as the increase in space velocity reduced the contact time of the reactant gases with the catalysts (Fig. 4e and f). However, interestingly, the U-(Cs)Ni/Al_2O_3 nanocatalyst still had a high CH_4 conversion of 82.7% and a CO_2 conversion of 87.5%, whereas the U-Ni/Al_2O_3 nanocatalyst did not maintain the reaction due to reactor clogging by the carbon-deposited catalyst. On the other hand, the commercial Ni catalyst showed largely decreased conversion rates of 40.6% of CH_4 and 54.8% of CO_2 at TOS = 4 h.

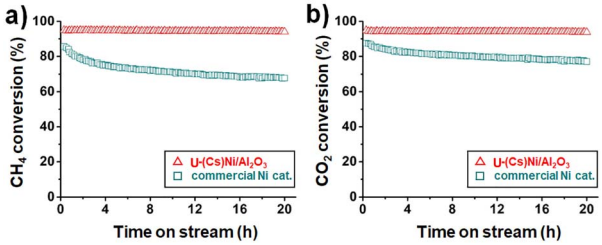

Fig. 5 (a) CH_4 and (b) CO_2 conversions of the catalysts in the long-term DRM reaction at 800 °C with a $CH_4/CO_2/N_2$ ratio = 1 : 1 : 2 under GHSV = 72 NL g_{cat}^{-1} h^{-1}.

In general, a high Ni loading of the catalyst can lead to an increased number of active sites if particle dispersion can be maintained. The uniform nanocatalyst with high Ni loading and high particle dispersion, prepared by using the automated AIO reaction system *via* a melt infiltration method, resulted in high conversion rates even under high GHSV conditions. U-(Cs)Ni/Al_2O_3 also achieved the highest syngas (H_2 and CO) productivity, calculated to be 6.89 mol_{H_2} g_{cat}^{-1} h^{-1} and 7.21 mol_{CO} g_{cat}^{-1} h^{-1}, respectively, at GHSV = 180 NL g_{cat}^{-1} h^{-1} (Fig. 4g and h). In particular, the hydrogen productivity of U-(Cs)Ni/Al_2O_3 at GHSV = 180 NL g_{cat}^{-1} h^{-1} was 2.58 times higher than that (2.67 mol_{H2} g_{cat}^{-1} h^{-1}) of the commercial Ni catalyst. Until now, most Ni-based catalysts with high coke resistance showed low conversions due to a low Ni content.[50] To both achieve high conversion rates and ensure coke resistance, conventional catalysts with a low metal content should be run under relatively low GHSV conditions.[51,52] However, the U-(Cs)Ni/Al_2O_3 nanocatalyst experienced high conversion rates as well as good stability with high coke resistance even under high GHSV conditions. To the best of our knowledge, this is an excellent value among DRM catalysts (Table S2†).

To verify the long-term stability of U-(Cs)Ni/Al_2O_3 and the commercial Ni catalyst, DRM reactions were also conducted for 20 h under GHSV = 72 NL g_{cat}^{-1} h^{-1} at 800 °C with a $CH_4/CO_2/N_2$ ratio = 1 : 1 : 2 (Fig. 5). The U-(Cs)Ni/Al_2O_3 nanocatalyst exhibited high and constant conversion rates, whereas the commercial Ni catalyst showed a significant deactivation trend during the reaction.

Investigation of the uniformity effect of active sites in the DRM reaction

For comparison with other conventional Ni-based catalysts, Ni particles and Cs-doped Ni particles were manually prepared on an alumina support by the incipient wetness impregnation (IWI) method. For the synthesis of IWI-(Cs)Ni/Al_2O_3 and IWI-Ni/Al_2O_3, the same Ni content as the automated uniform catalysts prepared with the AIO apparatus was applied.

The TEM images of the IWI-Ni/Al_2O_3 and IWI-(Cs)Ni/Al_2O_3 catalysts showed inhomogeneous particles consisting of some

Ni clumps around 30 nm and small Ni nanoparticles less than 5 nm (Fig. 6a and b). The TEM image and corresponding EDS line profile of IWI-Cs(Ni)/Al_2O_3 revealed an irregular distribution of Cs dopants on the Ni surface (Fig. 6b and c). IWI-Cs(Ni)/Al_2O_3 contained two separate regions of Cs-rich Ni and Cs-free Ni.

In the XRD data of IWI-Ni/Al_2O_3 and IWI-(Cs)Ni/Al_2O_3, there were sharper peaks at $2\theta = 44.5°$ in both cases compared to the U-(Cs)Ni/Al_2O_3 catalyst, which reflected the formation of larger Ni crystals (Fig. 6d). Therefore, the manual synthesis by incipient wetness impregnation methods for highly Ni-loaded catalysts yielded more irregular catalysts in terms of both Ni particle dispersion and Cs dopant distribution compared to the uniform catalysts prepared with the automated AIO reaction system.

The catalytic performance of the IWI-(Cs)Ni/Al_2O_3 and IWI-Ni/Al_2O_3 catalysts was also tested under GHSV = 72 NL g_{cat}^{-1} h^{-1} (Fig. 6e and f). Although the initial conversion rate for 60 min was very high for the IWI-Ni/Al_2O_3 catalyst, the reaction could not proceed any further after 80 min because of reactor clogging caused by severe carbon deposition of the catalysts. The Cs-doped IWI-(Cs)Ni/Al_2O_3 catalyst showed a slightly longer reaction time of 20 min than the Cs-free IWI-Ni/Al_2O_3 catalyst, but the reactor was also plugged by the generated carbon.

The TEM images of the spent catalysts recovered after 4 h of DRM reaction under the same harsh reaction conditions of GHSV = 72 NL g_{cat}^{-1} h^{-1} obviously showed the difference in coke resistance among the catalysts (Fig. 7). The spent U-(Cs)Ni/Al_2O_3 nanocatalyst maintained a uniform dispersion of Ni nanoparticles without any significant agglomeration (Fig. 7a). In addition, there were no carbon shells or filaments on the surface of active nickel nanoparticles, as shown in the HR-TEM image (Fig. 7b). On the other hand, the TEM images of the other catalysts (Cs-free U-Ni/Al_2O_3 nanocatalyst, commercial Ni catalyst, IWI-Ni/Al_2O_3, and IWI-(Cs)Ni/Al_2O_3) demonstrated carbon whiskers on the catalyst surface (Fig. 7c–f). In particular, there were more carbon whiskers in the catalysts produced by the incipient wetness method (Fig. 7e and f).

We investigated the different coke resistances between the U-(Cs)Ni/Al_2O_3 and IWI-(Cs)Ni/Al_2O_3 catalysts through DFT calculations by examining the reaction pathways and key elementary steps for coke formation during the DRM process. To describe the Ni surface with different Cs doping uniformity, we prepared Ni (111) slab structures with a different number of Cs dopants on the surface to represent the model structures for U-(Cs)Ni/Al_2O_3 and IWI-(Cs)Ni/Al_2O_3 nanocatalysts (Fig. 8a). The noted U-(Cs)Ni (111) and IWI-(Cs)Ni (111) refer to the surface model structures for U-(Cs)Ni/Al_2O_3 and IWI-(Cs)Ni/

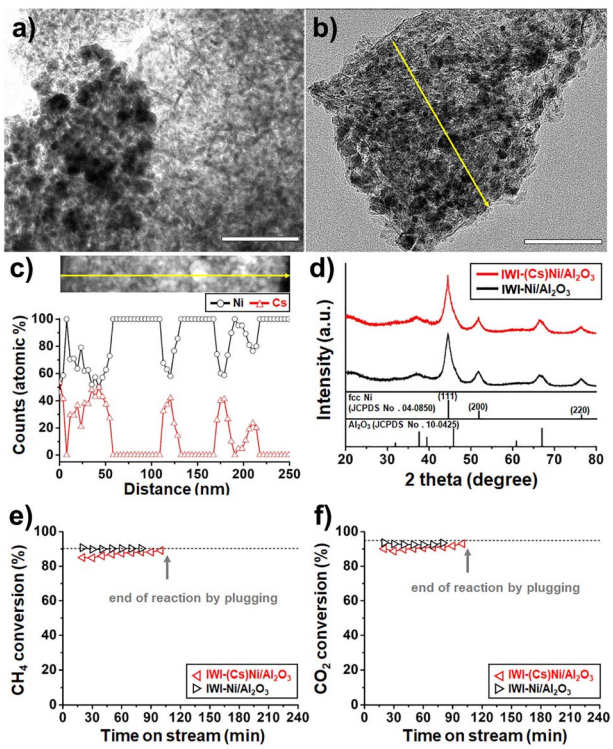

Fig. 6 (a) Low-resolution TEM image of IWI-Ni/Al_2O_3 and (b) TEM image and (c) corresponding EDS line profile with a HAADF-STEM image of the IWI-(Cs)Ni/Al_2O_3 catalyst. (d) XRD spectra of the catalysts. (e) CH_4 and (f) CO_2 conversions of the catalysts by the DRM reactions performed under GHSV = 72 NL g_{cat}^{-1} h^{-1} at 800 °C with a CH_4/CO_2 ratio of 1. The bars represent 100 nm (a and b).

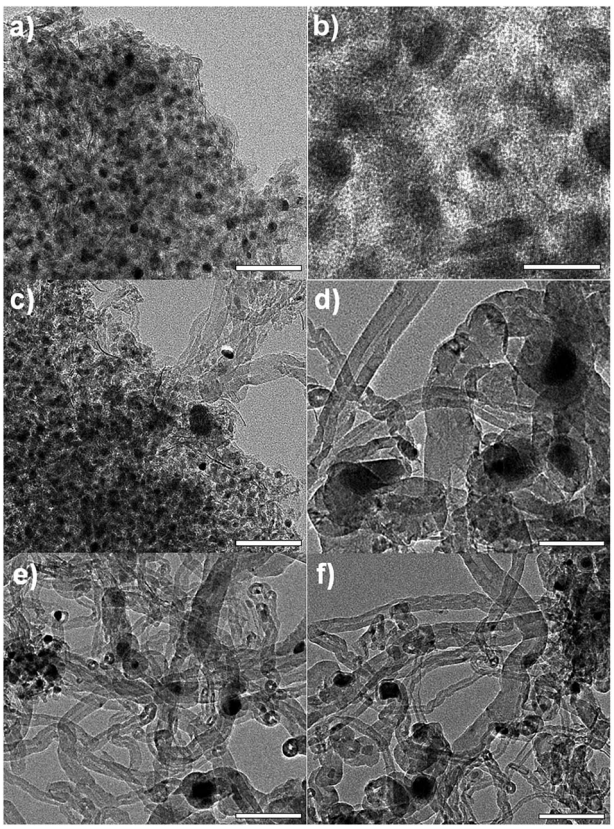

Fig. 7 (a–f) TEM images of the recovered catalysts under the same DRM reaction conditions recorded at 800 °C with a CH_4/CO_2 ratio of 1 under GHSV = 72 NL g_{cat}^{-1} h^{-1}. (a and b: the spent U-(Cs)Ni/Al_2O_3 nanocatalyst, (c): the spent U-Ni/Al_2O_3 nanocatalyst, (d): the spent commercial Ni catalyst, (e): the spent IWI-Ni/Al_2O_3, and (f): the spent IWI-(Cs)Ni/Al_2O_3). The bars represent 100 nm (a, c, d, e, and f) and 20 nm (b).

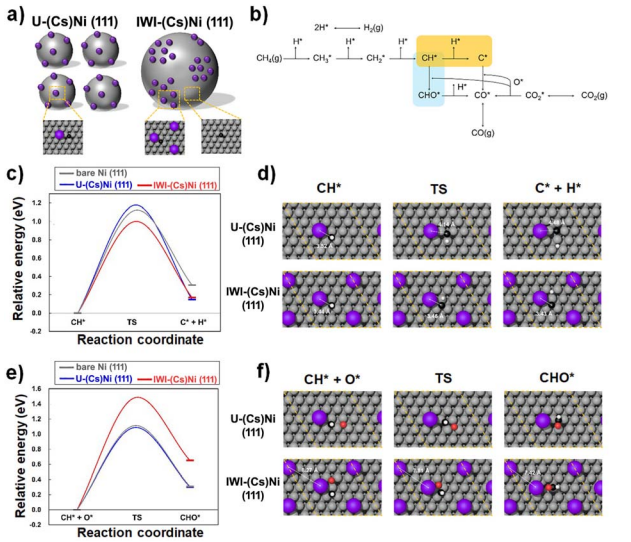

Fig. 8 (a) Atomistic representation of U-(Cs)Ni/Al_2O_3 and IWI-(Cs)Ni/Al_2O_3 showing different Cs uniformity. (b) Schematic diagram of the reaction pathway for the DRM. (c and d) Activation energy diagram for CH* dehydrogenation and its corresponding geometry-optimized atomic structures of initial, transition, and final states for U-(Cs)Ni(111) and IWI-(Cs)Ni (111). (e and f) Activation energy diagram for CH* oxidation and its corresponding geometry-optimized atomic structures. Grey, purple, black, red, and white balls represent Ni, Cs, C, O, and H atoms, respectively. Yellow dashed lines in the atomic structures indicate the supercell used in this work.

Al_2O_3. The Al_2O_3 substrate was omitted in the actual simulation to focus on the role of Cs on the Ni (111) surface.

It is generally accepted that surface carbon C* is a precursor for surface carbon deposition, so the carbon deposition resistance would increase if C* formation in the DRM process could be decreased.[53] The schematic diagram of the reaction pathway shows competitive reactions of CH* conversion as highlighted (Fig. 8b). One is the CH* dehydrogenation reaction (CH* + * → C* + H*) and the other is the CH* oxidation reaction (CH* + O* → CHO* + *). If the CHO* formation reaction in the CH* conversion is energetically more favorable than the C* formation reaction, the carbon deposition should be reduced.

For the bare Ni (111) surface, the activation energy barrier of the dehydrogenation step (CH* + * → C* + H*) and the oxidation step (CH* + O* → CHO* + *) was calculated to be 1.12 eV and 1.11 eV, respectively (Table 1 and Fig. S11†). The energy difference between two competitive reactions on the bare Ni (111) was almost negligible, which indicated that both reactions could simultaneously occur. However, for the U-(Cs)Ni (111) surface where a 1 Cs atom was doped on the 6 × 6 Ni (111) surface, the energy difference between the CH* oxidation step and dehydrogenation step was found to be increased to 0.1 eV, which leads to more favorable CH* oxidation (Table 1 and Fig. 8c and e). Moreover, the activation energy barrier of the CH* dehydrogenation step increased to 1.18 eV, which results in enhanced coke resistance. Interestingly, DFT calculations showed that the coke formation would be accelerated when the areal density of the Cs dopant increased, for example, in the case of IWI-(Cs)Ni (111) where there is a Cs-rich surface. For the IWI-(Cs)Ni (111) surface, the activation energy barrier of the dehydrogenation step and the oxidation step was respectively calculated to be 1.00 and 1.48 eV (Table 1 and Fig. 8c and e), indicating energetically favorable coke formation owing to the significantly lowered reaction barrier for the C* formation during the competitive reactions of CH* conversion.

Table 1 The calculated activation energy of CH* dehydrogenation and oxidation for bare Ni (111), U-(Cs)Ni (111), and IWI-(Cs)Ni (111) surfaces

	Adsorption energy (eV)		
Reaction	Bare Ni (111)	U-(Cs)Ni (111)	IWI-Ni(Cs)Ni (111)
CH* + * → C* + H*	1.12	1.18	1.00
CH* + O* → CHO* + *	1.11	1.08	1.48

This was due to the areal density of the Cs dopant, which changed the active sites for the CH* conversion. The geometry-optimized structures of the CH* dehydrogenation step showed that the most stable adsorption site of C on the IWI-(Cs)Ni (111) surface was an fcc hollow site while that on the U-(Cs)Ni (111) surface was an hcp hollow site (Fig. S12†). Since the CH molecule prefers to adsorb on an fcc hollow site irrespective of the Cs doping density, C–H bond breaking occurs after the CH molecule is moved to a nearby hcp hollow site, which requires additional energy and creates higher activation energy in the CH* dehydrogenation step for the U-(Cs)Ni (111) surface (Fig. 8d). In the meantime, for IWI-(Cs)Ni (111), the activation energy of CHO* formation was found to increase significantly since the Cs dopant needed to be pushed away from its stable site at the saddle point to form CHO*, which was energetically unfavorable due to the undesirable repulsive force between two closer Cs cations (Fig. 8f). All the calculated adsorption energies of the adsorbate and corresponding adsorption sites are summarized (Table S3†). Our DFT calculations suggest that the enhanced carbon deposition resistance for U-(Cs)Ni/Al_2O_3 was due to uniform Cs doping, which increased the activation energy barrier for CH* dehydrogenation over that for CH* oxidation, which is known to be the essential step for coke formation.

Conclusions

In this study, using an automated AIO reaction system *via* a facile melt infiltration method, we simply prepared a highly uniform and easily reproducible catalyst (U-(Cs)Ni/Al_2O_3), which contained homogeneously Cs-doped Ni nanoparticles (*ca.* 5 nm) with high Ni loading (*ca.* 30 wt%). The catalyst demonstrated a very high conversion rate and the best syngas productivity up to 6.89 mol_{H_2} g_{cat}^{-1} h^{-1} and 7.21 mol_{CO} g_{cat}^{-1} h^{-1} even in very harsh DRM reactions. In addition, a constant long-term reaction for 20 h was possible using the catalyst, based on its excellent thermal stability towards particle sintering and high carbon deposition resistance at 800 °C.

Computational simulations elucidated that the well-dispersed Cs dopant in the catalyst was able to effectively stabilize Ni nanoparticles, suppress CH* dehydrogenation, and enhance the CH* oxidation step. Based on the significantly improved catalytic properties in activity, productivity, and coke resistance of the catalyst as well as reliability, we anticipate that the proposed catalyst can optimize the sustainable production of syngas by a DRM reaction and thus reduce greenhouse gases.

Author contributions

Kyung Hee Oh: experiment & drafting; Jin Hee Lee: data curation & drafting; Kwangsoo Kim: DFT calculation; Hack-Keun Lee: data curation; Shin Wook Kang: investigation; Jung-Il Yang: visualization; Jong-Ho Park: visualization; Chang Seop Hong: conceptualization & editing; Byung-Hyun Kim: computer simulation & writing; Ji Chan Park: conceptualization & methodology & writing.

Conflicts of interest

There are no conflicts to declare.

Acknowledgements

This work was conducted within the framework of a research and development program of the Korea Institute of Energy Research (C2-2433) and funded by the National Research Foundation of Korea grant funded by the Korean government (NRF-2022M3H4A7085220).

Notes and references

1 N. W. Kwak, S. J. Jeong, H. G. Seo, S. Lee, Y. Kim, J. K. Kim, P. Byeon, S.-Y. Chung and W. Jung, *Nat. Commun.*, 2018, **9**, 4829.
2 J. Zhang, L. Wang, B. Zhang, H. Zhao, U. Kolb, Y. Zhu, L. Liu, Y. Han, G. Wang, C. Wang, D. S. Su, B. C. Gates and F.-S. Xiao, *Nat. Catal.*, 2018, **1**, 540.
3 S. Hu and W.-X. Li, *Science*, 2021, **374**, 1360.
4 M. Torimoto and Y. Sekine, Effects of alloying for steam or dry reforming of methane: a review of recent studies, *Catal. Sci. Technol.*, 2022, **12**, 3387.
5 Y. Yao, Z. Huang, T. Li, H. Wang, Y. Liu, H. S. Stein, Y. Mao, J. Gao, M. Jiao, Q. Dong, J. Dai, P. Xie, H. Xie, S. D. Lacey, I. Takeuchi, J. M. Gregoire, R. Jiang, C. Wang, A. D. Taylor, R. Shahbazian-Yassar and L. Hu, *Proc. Natl. Acad. Sci. U. S. A.*, 2020, **117**, 6316.
6 K. Potgieter, A. Aimon, E. Smit, F. v. Delft and R. Meijboom, *Chem.: Methods*, 2021, **1**, 192.
7 M.-S. Fan, A. Z. Abdullah and S. Bhatia, *ChemCatChem*, 2009, **1**, 192.
8 L. Chen, Z. Qi, S. Zhang, J. Su and G. A. Somorjai, *Catalysts*, 2020, **10**, 858.
9 S. Kawi, Y. Kathiraser, J. Ni, U. Oemar, Z. Li and E. T. Saw, *ChemSusChem*, 2015, **8**, 3556.
10 D. Pakhare and J. Spivey, *Chem. Soc. Rev.*, 2014, **43**, 7813.
11 S. Bhattar, M. A. Abedin, S. Kanitkar and J. J. Spivey, *Catal. Today*, 2021, **365**, 2.
12 J.-C. Seo, E. Cho, J. Kim, S. B. Kim, S. B. Kim, J.-R. Youn, D. H. Kim, P. K. Ramasamy, K. Lee and C. H. Ko, *J. Environ. Chem. Eng.*, 2022, **10**, 108058.
13 B.-J. Kim, J.-C. Seo, D.-H. Kim, Y.-L. Lee, K. Lee and H.-S. Roh, *J. CO2 Util.*, 2022, **58**, 101917.
14 J.-C. Seo, H. Kim, Y. L. Lee, S. C. Nam, H. S. Roh, K. Lee and S. B. Park, *ACS Sustainable Chem. Eng.*, 2021, **9**, 894.
15 Y. Song, E. Ozdemir, S. Ramesh, A. Adishev, S. Subramanian, A. Harale, M. Albuali, B. A. Fadhel, A. Jamal, D. Moon, S. H. Choi and C. T. Yavuz, *Science*, 2020, **367**, 777.
16 H.-K. Min, S. Kweon, Y. W. Kim, H. An, D. Jo, E. D. Park, C.-H. Shin and M. B. Park, *Appl. Catal., B*, 2021, **298**, 120627.
17 J. Oh, S. Joo, C. Lim, H. J. Kim, F. Ciucci, J.-Q. Wang, J. W. Han and G. Kim, *Angew. Chem., Int. Ed.*, 2022, **61**, e202204990.
18 Y. Liu, Y. Chen, Z. Gao, X. Zhang, L. Zhang, M. Wang, B. Chen, Y. Diao, Y. Li, D. Xiao, X. Wang, D. Ma and C. Shi, *Appl. Catal., B*, 2022, **307**, 121202.
19 J. W. Han, J. S. Park, M. S. Choi and H. Lee, *Appl. Catal., B*, 2017, **203**, 625.
20 M. A. A. Aziz, A. A. Jalil, S. Wongsakulphasatch and D.-V. N. Vo, *Catal. Sci. Technol.*, 2020, **10**, 35.
21 K. Mette, S. Kühl, A. Tarasov, M. G. Willinger, J. Kröhnert, S. Wrabetz, A. Trunschke, M. Scherzer, F. Girgsdies, H. Düdder, K. Kähler, K. F. Ortega, M. Muhler, R. Schlögl, M. Behrens and T. Lunkenbein, *ACS Catal.*, 2016, **6**, 7238.
22 J. Huang, Y. Yan, S. Saqline, W. Liu and B. Liu, *Appl. Catal., B*, 2020, **275**, 119109.
23 N. Abdel Karim Aramouni, J. Zeaiter, W. Kwapinski and M. N. Ahmad, *Energy Convers. Manage.*, 2017, **150**, 614.
24 J. C. Park, J. U. Bang, J. Lee, C. H. Ko and H. Song, *J. Mater. Chem.*, 2010, **20**, 1239.
25 F. Wang, B. Han, L. Zhang, L. Xu, H. Yu and W. Shi, *Appl. Catal., B*, 2018, **235**, 26.
26 M. Yu, Y. A. Zhu, Y. Lu, G. Tong, K. Zhu and X. Zhou, The Promoting Role of Ag in Ni–CeO_2 Catalyzed CH_4–CO_2 Dry Reforming Reaction, *Appl. Catal., B*, 2015, **165**, 43.
27 L. Xu, F. Wang, M. Chen, X. Fan, H. Yang, D. Nie and L. Qi, *J. CO2 Util.*, 2017, **18**, 1.
28 Z. Hou, O. Yokota, T. Tanaka and T. Yashima, *Appl. Catal., A*, 2003, **253**, 381.
29 R. Franz, T. Kühlewind, G. Shterk, E. A. Hamad, A. Parastaev, E. Uslamin, E. J. M. Hensen, F. Kapteijn, J. Gascon and E. A. Pidko, *Catal. Sci. Technol.*, 2020, **10**, 3965.
30 F. Arena, F. Frusteri and A. Parmaliana, *Appl. Catal., A*, 1999, **187**, 127.
31 K. H. Oh, H.-K. Lee, S. W. Kang, J.-I. Yang, G. Nam, T. Lim, S. H. Lee, C. S. Hong and J. C. Park, *J. Ind. Eng. Chem.*, 2022, **106**, 449.
32 C. Yu, Q. Xiong, K. Yang, H. Chen and F. Pan, *Adv. Mater. Technol.*, 2021, **6**, 2001036.
33 M. S. Ferrandon, C. Byron, G. Celik, Y. Zhang, C. Ni, J. Sloppy, R. A. McCormick, K. Booksh, A. V. Teplyakov and M. Delferro, *Appl. Catal., A*, 2022, **629**, 118379.

34 H. K. Lee, S. W. Kang, J. I. Yang, D. H. Chun, J. H. Lee, D. Oh, J. Ban, T. Jung, H. Jung and J. C. Park, *React. Chem. Eng.*, 2020, **5**, 1218.
35 D. Salley, G. Keenan, J. Grizou, A. Sharma, S. Martín and L. Cronin, *Nat. Commun.*, 2020, **11**, 2771.
36 S. Chen, J. Zaffran and B. Yang, *ACS Catal.*, 2020, **10**, 3074.
37 L. Foppa, T. Margossian, S. M. Kim, C. Müller, C. Copéret, K. Larmier and A. Comas-Vives, *J. Am. Chem. Soc.*, 2017, **139**, 17128.
38 J. Niu, F. Guo, J. Ran, W. Qi and Z. Yang, *Int. J. Hydrogen Energy*, 2020, **45**, 30267.
39 D. Cheng, F. R. Negreiros, E. Aprà and A. Fortunelli, *ChemSusChem*, 2013, **6**, 944.
40 G. Kresse and J. Hafner, *Phys. Rev. B: Condens. Matter Mater. Phys.*, 1993, **47**, 558.
41 P. E. Blöchl, *Phys. Rev. B: Condens. Matter Mater. Phys.*, 1994, **50**, 17953.
42 J. P. Perdew, K. Burke and M. Ernzerhof, *Phys. Rev. Lett.*, 1996, **77**, 3865.
43 S. Grimme, J. Antony, S. Ehrlich and H. Krieg, *J. Chem. Phys.*, 2010, **132**, 154104.
44 G. Henkelman, B. P. Uberuaga and H. Jónsson, *J. Chem. Phys.*, 2000, **113**, 9901.
45 T. M. Eggenhuisen, J. P. den Breejen, D. Verdoes, P. E. de Jongh and K. P. de Jong, *J. Am. Chem. Soc.*, 2010, **132**, 18318.
46 J. Ewbank, L. Kovarikc, F. Dialloa and C. Sievers, *Appl. Catal., A*, 2015, **494**, 57.
47 J. C. Park, D. H. Chun, J.-I. Yang, H.-T. Lee, S. Hong, G. B. Rhim, S. Jang and H. Jung, *RSC Adv.*, 2015, **5**, 44211.
48 H. Xin, H. Yang, X. Lei, X. Du, K. Zhou, D. Li and C. Hu, *Ind. Eng. Chem. Res.*, 2020, **59**, 17373.
49 M. Akri, A. El Kasmi, C. B. Dupeyrat and B. Qiao, *Catalysts*, 2020, **10**, 630.
50 J. Liu, H. Peng, W. Liu, X. Xu, X. Wang, C. Li, W. Zhou, P. Yuan, X. Chen, W. Zhang and H. Zhan, *ChemCatChem*, 2014, **6**, 2095.
51 C. Dai, S. Zhang, A. Zhang, C. Song, C. Shi and X. Guo, *J. Mater. Chem. A*, 2015, **3**, 16461.
52 Z. Bian and S. Kawi, *ChemCatChem*, 2017, **10**, 320.
53 J. Niu, Y. Wang, S. E. Liland, S. K. Regli, J. Yang, K. R. Rout, J. Luo, M. Rønning, J. Ran and D. Chen, *ACS Catal.*, 2021, **11**, 2398.